

Cosmological Forecasts from the Baryon Acoustic Oscillations in 21cm Intensity Mapping

Benjamin Ostergaard¹, André A. Costa^{1,2,3*}, Yu Sang¹

¹Center for Gravitation and Cosmology, College of Physical Science and Technology, Yangzhou University, Yangzhou 225009, China

²College of Physics, Nanjing University of Aeronautics and Astronautics, Nanjing 211106, China

³Instituto Federal de Educação, Ciência e Tecnologia de Minas Gerais, Campus Itabirito, Itabirito 35450-000, Brazil

Abstract: We use the baryon acoustic oscillation (BAO) feature in the angular power spectrum (APS) of the 21cm line of neutral hydrogen (HI) to constrain cosmological parameters. As the BAO shift parameter can only constrain the product of the Hubble constant and the sound horizon $H_0 r_s$, we combine our Fisher matrices with cosmic microwave background (CMB) Fisher matrices from the covariance of *Planck* telescope to break this degeneracy. In particular, we find that the best constraints we can get with this method are on the Hubble parameter h , and the dark energy parameters w_0 and w_a . Assuming a noise level as for the BINGO telescope, we find $\sigma_h = 0.0055$ (0.8%) in the Λ CDM model. For the w CDM model, we find $\sigma_h = 0.020$ (2.9%) and $\sigma_{w_0} = 0.075$ (7.5%). In the CPL parameterization, we find $\sigma_h = 0.029$ (4.4%), $\sigma_{w_0} = 0.40$ (40%), and $\sigma_{w_a} = 1.7$. Although these constraints improve those from *Planck* alone, we observe the BINGO data will be more significant for the w CDM model. We also observe the constraints from the BAO only is not as strong as using the whole 21cm angular power spectrum, but it is less susceptible to systematic effects.

Key words: cosmology, baryon acoustic oscillations, 21cm intensity mapping

1 Introduction

Baryon acoustic oscillations (BAOs) are sinusoidal oscillations found in the angular power spectra (APS) of both the cosmic microwave background (CMB) and galaxy and matter distribution. They are the result of overdensities in the primordial plasma. In the adiabatic model, the overdensity includes all particle species [1, 2]. Photons overpressure the region and drive a spherical sound wave carrying baryons along with it. The cold dark matter (CDM) does not interact with any other species and thus remains confined in a small radius. After decoupling, the sound wave freezes out as the sound speed decreases rapidly. We are left with a spherical baryon overdensity with a radius r_s and a CDM overdensity at the center of the sphere. These overdensities at both the sphere and its center grow by gravitational instability and provide the seeds for galaxy generation [1, 2].

Our universe is then composed of many superpositions of these spheres. Fortunately, the perturbation behave linearly at high redshifts so we can simply add them all together [2]. Of course, the sphere does not have zero thickness. There are three factors that determine its width: Photons leak out of the sound wave producing a phenomenon called Silk damping [3]; Over time the

inertia of the baryons relative to the photons increases thus changing the sound speed and broadening the wave adiabatically [2]; Finally, the initial perturbations can interfere with each other. Since galaxies are more likely to form on these spheres, we see a peak in the galaxy 2-point correlation function at about ~ 150 Mpc. This peak in the correlation function corresponds to an oscillation in the power spectrum, the Fourier transform of the correlation function.

In this paper, we use intensity maps of 21cm line of neutral hydrogen as a tracer for the matter angular power spectrum. The hydrogen atom is one of the simplest objects in atomic physics, simply consisting of a proton and an electron. In its ground 1S state, there are actually two “hyperfine” states related to the interaction of the proton and electron’s magnetic moments. A hydrogen atom in the excited hyperfine state, where both the spins of the proton and electron are aligned, can spontaneously decay into the lower hyperfine state where the electron’s spin “flips” and the two spins become antiparallel. The energy difference between these two states is $\Delta E = 5.9 \times 10^{-6}$ eV. Energy conservation leads to the difference being accounted for by a release of a photon with this energy. The corresponding wavelength and frequency of this photon are 21cm and 1420 MHz, respectively. Studies of hydrogen masers have pro-

Received 202x

* E-mail: andrealecardacosta@gmail.com (Corresponding author)

©2017 Chinese Physical Society and the Institute of High Energy Physics of the Chinese Academy of Sciences and the Institute of Modern Physics of the Chinese Academy of Sciences and IOP Publishing Ltd

vided very precise measurements of these quantities [4]. Thus, the 21cm line makes a great, well-understood astronomical probe.

The main difference between intensity mapping and galaxy surveys, the other major low-redshift observation technique, is that while galaxy surveys must resolve each individual galaxy and their redshifts, intensity mapping simply counts the number of photons that land on each pixel of the observation volume. Essentially, intensity mapping surveys are simply digital cameras. The instruments, data, and computing resources required for galaxy surveys such as the Sloan Digital Sky Survey [5] are astronomical. Conversely, the instruments required for intensity maps are relatively cheap and the data processing is easier. If we want to understand galaxy distributions from an intensity map, all we have to do is calculate and apply the bias to the power spectrum, a much easier task than individually resolving and calculating the redshift of every galaxy in the survey volume.

Because of these many advantages, there are several experiments under way to observe the 21cm signal specifically for the purpose of measuring BAOs. We mention a few: the Canadian Hydrogen Intensity Mapping Experiment (CHIME) [6], MeerKAT [7], the Square Kilometer Array (SKA) [8], and Baryon acoustic oscillations from Integrated Neutral Gas Observations (BINGO) [9–11].

We use specifications for the BINGO telescope in our analysis. A set of companion papers have been published describing the BINGO project. BINGO I [11] provides an overview of the project. BINGO II [12] provides a detailed instrument description. BINGO III [13] discusses the optical design and optimization of the focal plane. BINGO IV [14] simulates the mission and the preliminary steps for component separation. BINGO V [15] describes the full component separation and bispectrum analysis of the data. BINGO VI [16] provides a mock to test our data analysis on. BINGO VII [17] makes cosmological forecasts using the Fisher matrix method for the total angular power spectrum and assesses the BINGO setup and how it compares to other telescopes. BINGO VIII [18] discusses the recoverability of the BAO signal from HI intensity maps using the Markov Chain Monte Carlo method.

This paper is organized as follows. In Section 2, we derive the 21cm angular power spectrum we use in our analysis. In particular, we explain how we rewrite the APS given in BINGO VII [17] in terms of the 3D power spectrum $P(k)$ and extract the BAO shift parameter. In Section 3, we explain how we get cosmological parameters from the APS using a Fisher matrix analysis. We present our constraints from the BAO feature for three different models in Section 4 and compare our results with previous works. We discuss some errors with degeneracies and how we patch them with cosmic mi-

crowave background data. We make our conclusions and potential future work in Section 5.

2 BAO feature from the 21cm signal

The 21cm brightness temperature perturbation in direction \hat{n} is given in Ref. [19]

$$\Delta_{T_b}(z, \hat{n}) = \delta_n - \frac{1}{\mathcal{H}} \left[\hat{n} \cdot (\hat{n} \cdot \vec{\nabla}) \vec{v} \right] + \left(\frac{d \ln(a^3 \bar{n}_{\text{HI}})}{d\eta} - \frac{\dot{\mathcal{H}}}{\mathcal{H}} - 2\mathcal{H} \right) \delta\eta + \frac{1}{\mathcal{H}} \dot{\Phi} + \Psi, \quad (1)$$

where δ_n is the HI density perturbation, \mathcal{H} is the Hubble parameter in conformal time, \vec{v} is the peculiar velocity, \bar{n}_{HI} is the average HI number density, and Ψ and Φ are the gravitational perturbation functions. Overdots indicate derivatives with respect to conformal time.

We then decompose this into spherical harmonics [17, 19]

$$\Delta_{T_b}(z, \hat{n}) = \sum_{lm} \Delta_{T_b,lm}(z) Y_{lm}(\hat{n}). \quad (2)$$

We write the coefficients $\Delta_{T_b,lm}(z)$ in terms of the Fourier transforms of the perturbations

$$\Delta_{T_b,lm}(z) = 4\pi i^l \int \frac{d^3 \vec{k}}{(2\pi)^{3/2}} \Delta_{T_b,l}(\vec{k}, z) Y_{lm}^*(\hat{k}), \quad (3)$$

where

$$\begin{aligned} \Delta_{T_b,l}(\vec{k}, z) &= \delta_n j_l(k\chi) + \frac{kv}{\mathcal{H}} j_l''(k\chi) + \left(\frac{1}{\mathcal{H}} \dot{\Phi} + \Psi \right) j_l(k\chi) \\ &\quad - \left[\frac{1}{\mathcal{H}} \frac{d \ln(a^3 \bar{n}_{\text{HI}})}{d\eta} - \frac{\dot{\mathcal{H}}}{\mathcal{H}^2} - 2 \right] \\ &\quad \times \left[\Psi j_l(k\chi) + v j_l'(k\chi) + \int_0^\chi (\dot{\Psi} + \dot{\Phi}) j_l(k\chi') d\chi' \right], \end{aligned} \quad (4)$$

where $j_l(k\chi)$ are the spherical Bessel functions and primes on the Bessel functions denote derivatives with respect to the argument.

To get the data over some redshift bin we integrate over the redshift-normalized window function $W(z)$ [17]

$$\Delta_{T_b,l}^W(\vec{k}) = \int_0^\infty dz \bar{T}_b(z) W(z) \Delta_{T_b,l}(\vec{k}, z). \quad (5)$$

The angular power spectrum is then defined as [19]

$$C_l^{WW'} = 4\pi \int d \ln k \mathcal{P}_{\mathcal{R}}(k) \Delta_{T_b,l}^W(\vec{k}, z) \Delta_{T_b,l}^{W'}(\vec{k}, z), \quad (6)$$

where $\mathcal{P}_{\mathcal{R}}$ is the dimensionless power spectrum of the primordial curvature perturbation \mathcal{R} .

The biggest advantage of the 21cm C_l 's over CMB C_l 's is that because they are defined over different redshift bins, they allow for a tomographic analysis. More specifically we can explicitly see how the matter distribution of the universe evolves over time. Figure 1 shows

the 21cm C_l 's calculated for the 30 redshift bins used by the BINGO telescope. Going from higher redshifts (red) to lower redshifts (blue) we can observe three characteristics: first, as expected, matter structures grow and the power spectra increase especially at lower multipoles; second, the BAO scale moves to lower multipoles (larger angles), which means it increases with redshift; third, there is a suppression at higher multipoles. The BAO feature is easily identified as the ‘‘Wiggle’’ present across all redshifts.

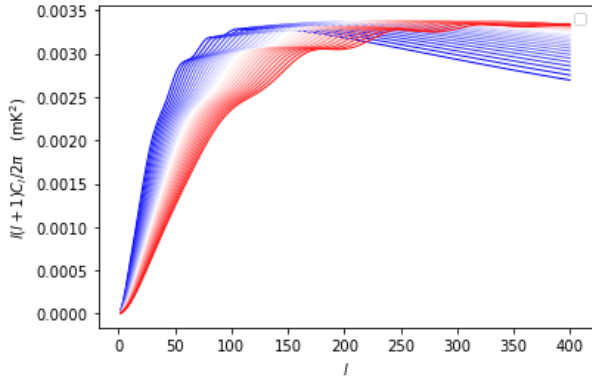


Fig. 1: Angular power spectra plotted over 30 redshift bins from $z = 0.13$ (blue) to $z = 0.44$ (red).

While Eq. (6) does give us the angular power spectrum for the 21cm distribution, we want a form of the APS that is given in terms of the matter power spectrum $P(k)$. Fortunately, this is easy to do with a few substitutions.

First, as noted in Hall et al. (2013) [19], the first two terms in Eq. (4) are several orders of magnitude larger than the other components. Therefore, we will restrict our calculations to these two contributions only. Second, we can solve the velocity in terms of the density, such that we rewrite the brightness temperature perturbation as [20]

$$\Delta_{T_b,l}(\vec{k}, z) = (b_{\text{HI}} j_l(k\chi) - f(z) j_l''(k\chi)) D(z) \delta_m(0, k), \quad (7)$$

where $D(z)$ and $f(z) \equiv d \ln D(z) / d \ln a$ are the growth function and growth rate, respectively. Taking the density component today outside $\Delta_{T_b,l}(\vec{k}, z)$, we write the angular power spectra as [18]

$$C_l^{WW'} = \frac{2}{\pi} \int dk \Delta_{T_b,l}^W(\vec{k}, z) \Delta_{T_b,l}^{W'}(\vec{k}, z) k^2 P(k), \quad (8)$$

where $P(k)$ is the 3D matter power spectrum today, which is related to the transfer function $T(k)$ by [21]

$$P(k) = \delta_H^2 \frac{2\pi^2}{k^3} \left(\frac{ck}{H_0} \right)^{3+n} T^2(k), \quad (9)$$

where δ_H is the density perturbation at horizon crossing.

We use a numerical fit for the transfer function as given by Eisenstein and Hu (1998) [22]. This fit works in the linear regime, thus the power spectra is linear as well. To account for the growth of nonlinear structure, we make a template power spectrum [18, 23]

$$P_{\text{temp}}(k) = [P_{\text{lin}}(k) - P_{\text{nw}}(k)] e^{-k^2 \Sigma_{nl}^2} + P_{\text{nw}}(k), \quad (10)$$

where $\Sigma_{nl} = 5.2 \text{Mpc}/h$ is the nonlinear damping scale given by [24]. We use this equation for $P(k)$ in Eq. (8). Figure 2 shows the C_l 's obtained from inserting $P_{\text{temp}}(k)$, P_{lin} , and P_{nw} into Eq. 8, and also the effect of the template on the BAO scale alone.

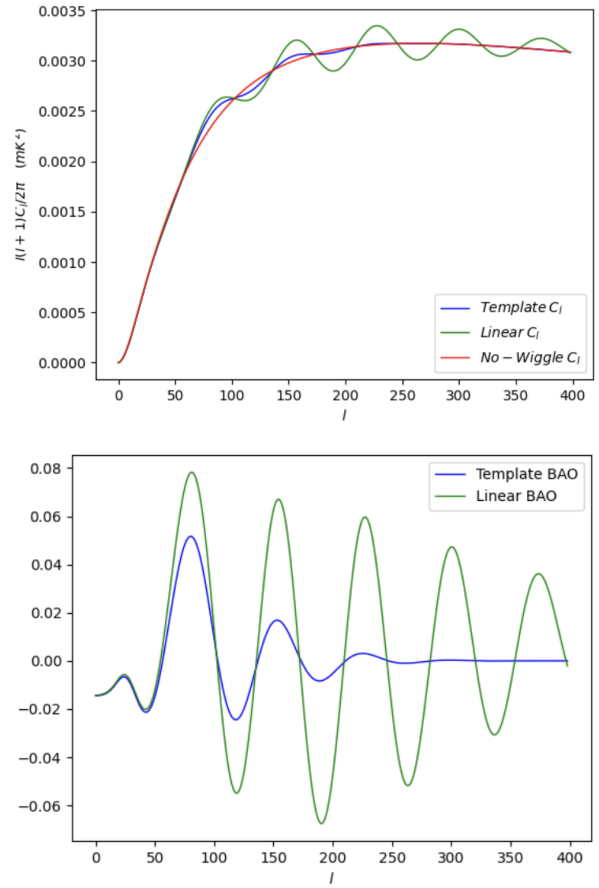


Fig. 2: (Upper panel) Comparison of C_l^{temp} (blue), C_l^{nw} (red), and C_l^{lin} (green). The difference between C_l^{temp} and C_l^{lin} is the nonlinear damping which suppresses the oscillations at higher multipoles. (Lower panel) BAO scale alone obtained by subtracting the C_l 's by the C_l^{nw} .

We intend to extract from the 21cm intensity maps the scale associated with the BAO feature, which is encoded in the angular diameter distance $d_A(z)$. Following [23], we use a template method and write the power spectrum signal as

$$C(l) = B_0 C_{\text{temp}}(l/\alpha) + A_0 + A_1 l + A_2 / l^2, \quad (11)$$

where B_0 and A_i are nuisance parameters. Specifically, the amplitude B_0 is related to the linear bias squared and the parameters A_i account for scale-dependent bias, shot noise, uncertainties in the redshift space distortion, etc. We set the fiducial values as $B_0 = 1$ and $A_i = 0$, and allow them to vary with redshift.

Most importantly, Eq. (11) has a much more powerful feature than just allowing us to account for more sources of error. The shift parameter α measures the shift of the BAO peak positions with respect to our fiducial cosmology. It is defined as [23]

$$\alpha \equiv \frac{(d_A(z)/r_s)}{(d_A(z)/r_s)_{\text{fid}}}, \quad (12)$$

where $d_A(z)$ is the angular diameter distance and r_s is the sound horizon at drag epoch. Measuring α is a very good test for how accurate a fiducial cosmology is. Not only that, but α only depends on the BAO effect, it is completely independent of bias and other parameters meaning that we only have to understand BAO physics well to get accurate cosmological constraints.

3 Fisher Matrix Analysis

For a set of parameters θ_i and a model \mathcal{M} , the Fisher information matrix can be calculated as [25]

$$F_{ij} \equiv \left\langle \frac{\partial^2 \mathcal{L}}{\partial \theta_i \partial \theta_j} \right\rangle = \frac{1}{2} \text{Tr} \left[\mathbf{C}^{-1} \frac{\partial \mathbf{C}}{\partial \theta_i} \mathbf{C}^{-1} \frac{\partial \mathbf{C}}{\partial \theta_j} \right], \quad (13)$$

where $\mathcal{L} = -\ln L$ and L is the likelihood function.

We write the covariance \mathbf{C} as the sum of the template C_i s and the noise spectra

$$\mathbf{C} = C(l) + C_i^{\text{shot}}(z_i, z_j) + N_l(z_i, z_j), \quad (14)$$

where $C_i^{\text{shot}}(z_i, z_j)$ and $N_l(z_i, z_j)$ are respectively the shot and thermal noise given in [17].

We follow a similar approach to the CMB case, where we decompose the brightness temperature perturbation in spherical harmonics [18].

We note however that the CMB signal comes from one specific redshift and yields a 2-dimensional map, while 21cm surveys spans a whole volume and are 3-dimensional with multiple redshifts. Then, the CMB diagonal matrix is transformed into the block diagonal matrix [17]

$$C = \begin{bmatrix} A_{l=2} & 0 & \dots & 0 \\ 0 & A_3 & \dots & 0 \\ \vdots & \vdots & \dots & \vdots \\ 0 & 0 & \dots & A_n \end{bmatrix}, \quad (15)$$

where

$$A_l = (2l+1) \begin{bmatrix} C_l(z_1, z_1) & C_l(z_1, z_2) & \dots & C_l(z_1, z_n) \\ C_l(z_2, z_1) & C_l(z_2, z_2) & \dots & C_l(z_2, z_n) \\ \vdots & \vdots & \dots & \vdots \\ C_l(z_n, z_1) & C_l(z_n, z_2) & \dots & C_l(z_n, z_n) \end{bmatrix}. \quad (16)$$

Finally, if we have a Fisher matrix, F_{ij} , defined in terms of variables $\vec{\Theta} = (\theta_1, \theta_2, \dots, \theta_n)$, we can transform to a new Fisher matrix, F'_{kl} , defined in terms of variables $\vec{\Theta}' = (\theta'_1, \theta'_2, \dots, \theta'_m)$ for $m \leq n$ using the equation [26]

$$F'_{kl} = \sum_{ij} \frac{\partial \theta_i}{\partial \theta'_k} \frac{\partial \theta_j}{\partial \theta'_l} F_{ij}. \quad (17)$$

4 Results

Our fiducial cosmological parameters come from Planck 2018 [27] and are given in Table 1.

Table 1: Fiducial values for cosmological parameters. b_{HI} and Ω_{HI} are related to 21cm physics. B_0 , A_i , and α are the C_l template parameters.

Parameter	Fiducial Value
$\Omega_b h^2$	0.022383
$\Omega_c h^2$	0.12011
h	0.6732
n_s	0.96605
A_s	2.1×10^{-9}
w_0	-1
w_a	0
b_{HI}	1
Ω_{HI}	6.2×10^{-4}
B_0	1
A_i	0
α	1

We make our analysis in two steps. First, we calculate the Fisher matrix using the covariance for the template angular power spectra given by Eqs. (14) and (11). We take the BAO shift parameter α and the nuisance parameters B_0 and A_i , and allow them to assume different values by assuming an independent constant every three redshift bins over the 30 bins of our survey. This gives us a total of 50 parameters, 10 useful α s and 40 nuisance parameters. We do this for two reasons. Firstly, allowing the α to assume different values in different bins makes it possible to study its evolution with redshift. The second reason is that we ultimately want to transform our Fisher matrix of template variables into a Fisher matrix of physical variables given in Table 1. Since we can only

transform Fisher matrices into other Fisher matrices of the same size or smaller, we must ensure we start out with enough parameters. Splitting the parameters across redshift bins not only gives us more parameters. It also allows us to investigate how these parameters vary over time.

We use these 50 parameters to calculate a 50×50 Fisher matrix, which can be done using Eq. (13), setting all α s, B_0 s, and A_i s to their fiducial values, and calculating the derivatives numerically. This is the most computationally intensive step in our analysis by far. Since B_0 and the A_i s are nuisance parameters, we marginalize over them. That means we allow these parameters to assume any possible values and take into account their effect into the uncertainties of α s. We are left with a 10×10 Fisher matrix consisting of 10 α s split over 30 redshift bins from BINGO (so the bins have to share some α s). Finally, we then take the inverse of the Fisher matrix to get the covariance matrix. Taking the square root of the diagonal entries gives us the standard deviation of all 10 α s. We then average these 10 σ_{α} s across 3 redshift bins to get the results shown in Table 2. For comparison, we also include σ_{α} s from the Markov Chain Monte Carlo method from BINGO VIII [18].

Table 2: Standard deviations for α across 3 redshift bins. Markov Chain Monte Carlo results are from BINGO VIII [18].

z-bins	$\langle \sigma_{\alpha} \rangle$ Fisher	$\langle \sigma_{\alpha} \rangle$ MCMC
1-10	0.0816	0.0653
11-20	0.0636	0.0410
21-30	0.0508	0.0322

The second step in our analysis consists in transforming our constraints in the BAO shift parameters into constraints in the final cosmological parameters. As we saw in Eq. (12), the shift parameter α depends on the angular diameter distance and the sound horizon at the drag epoch, which are ultimately functions of $\Omega_b h^2$, $\Omega_c h^2$, h , and the dark energy equation of state parameters w_0 and w_a . Therefore, the uncertainties in α s can be related to uncertainties in these parameters, which can be done by transforming our 10×10 α Fisher matrix into a Fisher matrix for our final cosmological parameters.

And it is insensitive to $\ln(10^{10} A_s)$, n_s , b_{HI} , and Ω_{HI} . The fact that the BAO shift parameter is insensitive to the bias b_{HI} and the neutral hydrogen density Ω_{HI} is the main benefit of this approach over considering the full angular power spectra in our Fisher matrix analysis.

Table 3: Cosmological constraints for Λ CDM.

	<i>Planck</i>	BINGO VII + <i>Planck</i>	BINGO BAO + <i>Planck</i>
Parameter	$\pm 1\sigma (100\% \times \sigma / \theta_i^{\text{fid}})$	$\pm 1\sigma (100\% \times \sigma / \theta_i^{\text{fid}})$	$\pm 1\sigma (100\% \times \sigma / \theta_i^{\text{fid}})$
$\Omega_b h^2$	0.00015 (0.7%)	0.00013 (0.6%)	0.00014 (0.6%)
$\Omega_c h^2$	0.0014 (1.1%)	0.0010 (0.8%)	0.0012 (1.0%)
h	0.0061 (0.9%)	0.0045 (0.7%)	0.0055 (0.8%)
$\ln(10^{10} A_s)$	0.016 (0.5%)	0.015 (0.5%)	0.016 (0.5%)
n_s	0.0043 (0.4%)	0.0039 (0.4%)	0.0041 (0.4%)

Table 4: Cosmological constraints for w CDM.

	<i>Planck</i>	BINGO VII + <i>Planck</i>	BINGO BAO + <i>Planck</i>
Parameter	$\pm 1\sigma (100\% \times \sigma / \theta_i^{\text{fid}})$	$\pm 1\sigma (100\% \times \sigma / \theta_i^{\text{fid}})$	$\pm 1\sigma (100\% \times \sigma / \theta_i^{\text{fid}})$
$\Omega_b h^2$	0.00015 (0.7%)	0.00014 (0.6%)	0.00015(0.7%)
$\Omega_c h^2$	0.0014 (1.2%)	0.0011 (0.9%)	0.0014 (1.2%)
h	0.089 (13%)	0.0073 (1.1%)	0.020 (2.9%)
$\ln(10^{10} A_s)$	0.016 (0.5%)	0.016 (0.5%)	0.0016 (0.5%)
n_s	0.0044 (0.5%)	0.0040 (0.4%)	0.0043 (0.4%)
w_0	0.26 (25%)	0.033 (3.3%)	0.075 (7.5%)

Table 5: Cosmological constraints for CPL.

	<i>Planck</i>	BINGO VII + <i>Planck</i>	BINGO BAO + <i>Planck</i>
Parameter	$\pm 1\sigma (100\% \times \sigma / \theta_i^{fid})$	$\pm 1\sigma (100\% \times \sigma / \theta_i^{fid})$	$\pm 1\sigma (100\% \times \sigma / \theta_i^{fid})$
$\Omega_b h^2$	0.00016 (0.7%)	0.00014 (0.6%)	0.00015 (0.7%)
$\Omega_c h^2$	0.0013 (1.1%)	0.0011 (0.9%)	0.0013 (1.1%)
h	0.088 (13%)	0.019 (2.9%)	0.029 (4.4%)
$\ln(10^{10} A_s)$	0.016 (0.5%)	0.016 (0.5%)	0.016 (0.5%)
n_s	0.0044 (0.5%)	0.0041 (0.4%)	0.0044 (0.5%)
w_0	0.46 (46%)	0.30 (30%)	0.40 (40%)
w_a	1.8	1.2	1.7

Unfortunately, as discussed in [28], there is a large degeneracy between H_0 and r_d using the BAO data only, and we can only determine the combination $H_0 r_s$. In order to break this degeneracy, we need prior knowledge about $\Omega_b h^2$. This can be done by combining the BAO data with some external data which properly constrain this parameter. Therefore, we combine our Fisher matrix results from the 21cm intensity mapping with the Fisher matrix obtained from CMB data by the Planck telescope. We do this for three cosmic acceleration models Λ CDM, w CDM, and CPL ($w_0 w_a$ CDM). Our results are shown in Tables 3, 4, and 5 for Λ CDM, w CDM, and CPL, respectively.

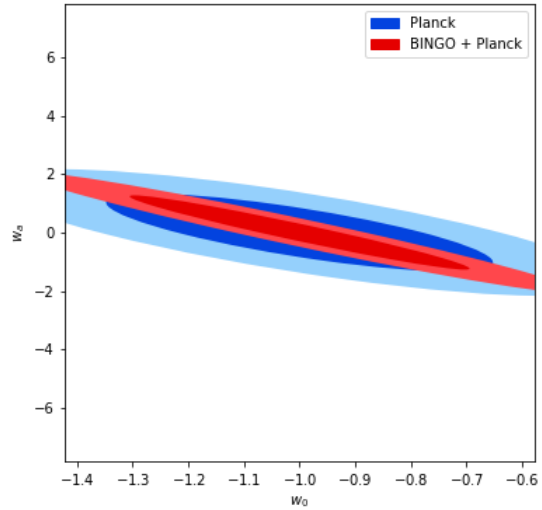


Fig. 4: Marginalized 68% and 95% Confidence Ellipses for w_0 and w_a in the CPL model.

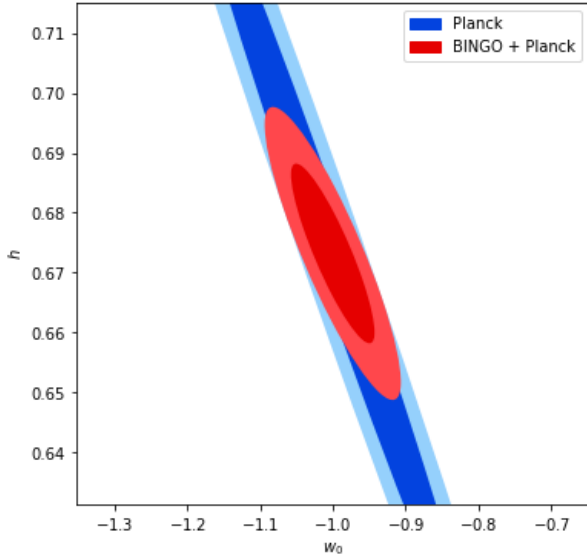


Fig. 3: Marginalized 68% and 95% Confidence Ellipses for w_0 and h in the w CDM model.

In most cases, The combined BINGO BAO + Planck constraints are not statistically any stronger than the constraints from Planck alone. However, the constraints for h , w_0 , and w_a do get improved significantly over Planck. This makes sense as more data related to cosmic expansion is encoded in late-time 21cm data than in early-time CMB data. Unfortunately, these constraints are not as strong as those obtained by calculating the Fisher matrix from the entire 21cm angular power spectrum as done in BINGO VII [17]. Figure 3 shows the confidence ellipses for w_0 and h in the w CDM model for both Planck and BINGO BAO + Planck. Figure 4 shows the confidence ellipses for w_0 and w_a in the CPL model.

5 Discussions and Conclusions

We have found that calculating a Fisher matrix of a template power spectrum is capable of putting constraints on the BAO peak shift parameter α with results comparable to, but slightly less optimistic than,

the MCMC analysis in BINGO VIII [18]. It is not clear for us why the MCMC result produces better results in this case, but this makes our analysis more conservative. Unlike the MCMC analysis, the Fisher matrix method does not calculate the best fit values for the parameters, however, it is significantly less computationally intensive.

We have also found that transforming this Fisher matrix into a Fisher matrix of cosmological parameters is far to degenerate to give any useful constraints on its own. It has actually been demonstrated, e.g. in the DESI collaboration [28], that the only cosmological constraints that can be obtained from BAO alone in a flat Λ CDM model are in the Ω_m and $H_0 r_d$. Because of this, we combine the BAO information with CMB data to introduce a prior in $\Omega_b h^2$ and break those degeneracies. Our results show that the BAO data will mainly constrain the hubble parameter h and the dark energy equation of state parameters w_0 and w_a . In fact, the best results were obtained for the w CDM model, which improved the constraints of the Planck satellite from

$h = 0.089$ (13%) and $w_0 = 0.26$ (25%) to $h = 0.020$ (2.9%) and $w_0 = 0.075$ (7.5%). This result is consistent with what was obtained by Olivari et al. [29], although they used a different methodology to extract the BAO information.

We also compare our analysis with the results from the full angular power spectra obtained in BINGO VII [17]. As expected, the full power spectra contains more information than the BAO wiggles alone. Therefore, our constraints were at the same level or worse than the previous analysis. However, the BAO do not depend on the overall amplitude of the 21cm angular power spectra, which makes it less susceptible to systematic effects from foregrounds removal, bias, and non-linearities.

Acknowledgements

Supported by the National Natural Science Foundation of China (12175192, 12005184).

References

- 1 P. J. E. Peebles and J. T. Yu. Primeval adiabatic perturbation in an expanding universe. *Astrophysical Journal*, 162:815–836, 1970.
- 2 Daniel J. Eisenstein, Hee-Jong Seo, and Martin White. On the robustness of the acoustic scale in the low-redshift clustering of matter. *The Astrophysical Journal*, 664(2):660–674, August 2007.
- 3 Joseph Silk. Cosmic black body radiation and galaxy formation. *Astrophys. J.*, 151:459–471, 1968.
- 4 H. M. Goldenberg, D. Kleppner, and N. F. Ramsey. Atomic hydrogen maser. *Phys. Rev. Lett.*, 5:361–362, 10 1960.
- 5 Donald G. York et al. The Sloan Digital Sky Survey: Technical Summary. *Astron. J.*, 120:1579–1587, 2000.
- 6 M. Amiri et al. The CHIME Fast Radio Burst Project: System Overview. 3 2018.
- 7 Mario G. Santos et al. MeerKLASS: MeerKAT Large Area Synoptic Survey. In *MeerKAT Science: On the Pathway to the SKA*, 9 2017.
- 8 A. Weltman et al. Fundamental physics with the Square Kilometre Array. *Publ. Astron. Soc. Austral.*, 37:e002, 2020.
- 9 R. A. Battye, I. W. A. Browne, C. Dickinson, G. Heron, B. Maffei, and A. Pourtsidou. Hi intensity mapping: a single dish approach. *Monthly Notices of the Royal Astronomical Society*, 434(2):1239–1256, July 2013.
- 10 M.-A. Bigot-Sazy, C. Dickinson, R. A. Battye, I. W. A. Browne, Y.-Z. Ma, B. Maffei, F. Noviello, M. Remazeilles, and P. N. Wilkinson. Simulations for single-dish intensity mapping experiments. *Monthly Notices of the Royal Astronomical Society*, 454(3):3240–3253, 10 2015.
- 11 Elcio Abdalla et al. The BINGO project - I. Baryon acoustic oscillations from integrated neutral gas observations. *Astron. Astrophys.*, 664:A14, 2022.
- 12 Carlos A. Wuensche et al. The BINGO project - II. Instrument description. *Astron. Astrophys.*, 664:A15, 2022.
- 13 Filipe B. Abdalla et al. The BINGO Project - III. Optical design and optimization of the focal plane. *Astron. Astrophys.*, 664:A16, 2022.
- 14 Vincenzo Liccardo et al. The BINGO project - IV. Simulations for mission performance assessment and preliminary component separation steps. *Astron. Astrophys.*, 664:A17, 2022.
- 15 Karin S. F. Fornazier et al. The BINGO project - V. Further steps in component separation and bispectrum analysis. *Astron. Astrophys.*, 664:A18, 2022.
- 16 Jiajun Zhang et al. The BINGO project - VI. HI halo occupation distribution and mock building. *Astron. Astrophys.*, 664:A19, 2022.
- 17 Andre A. Costa et al. The BINGO project - VII. Cosmological forecasts from 21 cm intensity mapping. *Astron. Astrophys.*, 664:A20, 2022.
- 18 Camila Paiva Novaes et al. The BINGO project - VIII. Recovering the BAO signal in HI intensity mapping simulations. *Astron. Astrophys.*, 666:A83, 2022.
- 19 Alex Hall, Camille Bonvin, and Anthony Challinor. Testing general relativity with 21-cm intensity mapping. *Physical Review D*, 87(6), March 2013.
- 20 Scott Dodelson. *Modern cosmology*. Academic Press, 2003.
- 21 Emory F. Bunn and Martin White. The 4 year cobenormalization and large-scale structure. *The Astrophysical Journal*, 480(1):6–21, May 1997.
- 22 Daniel J. Eisenstein and Wayne Hu. Baryonic features in the matter transfer function. *The Astrophysical Journal*, 496(2):605–614, April 1998.
- 23 H. Camacho et al. Dark Energy Survey Year 1 Results: Measurement of the Galaxy Angular Power Spectrum. *Mon. Not. Roy. Astron. Soc.*, 487(3):3870–3883, 2019.
- 24 K. C. Chan et al. BAO from Angular Clustering: Optimization and Mitigation of Theoretical Systematics. *Mon. Not. Roy. Astron. Soc.*, 480(3):3031–3051, 2018.
- 25 Max Tegmark, Andy N. Taylor, and Alan F. Heavens. Karhunen-loeve eigenvalue problems in cosmology: How should we tackle large data sets? *The Astrophysical Journal*, 480(1):22–35, May 1997.
- 26 Dan Coe. Fisher matrices and confidence ellipses: A quick-start guide and software, 2009.
- 27 N. Aghanim et al. Planck 2018 results. VI. Cosmological pa-

- rameters. *Astron. Astrophys.*, 641:A6, 2020. [Erratum: *Astron. Astrophys.* 652, C4 (2021)].
- 28 A. G. Adame et al. DESI 2024 VI: Cosmological Constraints from the Measurements of Baryon Acoustic Oscillations. 4 2024.
- 29 L. C. Olivari, C. Dickinson, R. A. Battye, Y-Z. Ma, A. A. Costa, M. Remazeilles, and S. Harper. Cosmological parameter forecasts for HI intensity mapping experiments using the angular power spectrum. *Mon. Not. Roy. Astron. Soc.*, 473(3):4242–4256, 2018.